

Dynamics in Complex Fluids

Michele Cespa

19th March 2025

Abstract

Colloidal suspensions are known to exhibit stochastic behaviour with dependence on physical features of the system, including colloid size, fluid viscosity and temperature. Information of these stochastic processes can be retrieved from light scattering. In this investigation, two such methods were employed: DLS (Dynamic Light Scattering) and DDM (Differential Dynamic Microscopy). DLS involves constructing a discrete time intensity autocorrelation function at fixed scattering angles, which scales with $|\gamma(\vec{q}, t)|^2$ (the canonical autocorrelation). DDM instead utilises high frame rate video to construct an Image Structure Function (ISF) which also contains a $\gamma(\vec{q}, t)$ term from which information is recovered. DLS was run on polystyrene particles of diameter $0.51 \mu\text{m}$, $0.746 \mu\text{m}$, $1.06 \mu\text{m}$ yielding estimates of $0.45 \pm 0.07 \mu\text{m}$, $0.71 \pm 0.14 \mu\text{m}$, $0.77 \pm 0.16 \mu\text{m}$ respectively. DDM was run on $2.07 \mu\text{m}$ and $3.1 \mu\text{m}$ beads yielding estimates of $2.29 \pm 0.04 \mu\text{m}$ and $4.63 \pm 0.07 \mu\text{m}$, whilst for the smaller sizes (the same used for DLS) it yielded estimates of $0.50 \pm 0.02 \mu\text{m}$, $0.84 \pm 0.03 \mu\text{m}$, $1.16 \pm 0.04 \mu\text{m}$.

1 Introduction

Light scattering techniques on colloid suspensions rose to popularity in the 1970s with the advent of low tolerance lasers and adequate camera equipment. Many early contributions to Dynamic Light Scattering in particular can be attributed to Peter Pusey [1]. The underlying theory of the topic shall now be discussed (see John Berne and Robert Pecora's seminal textbook for a more thorough treatment [2]):

The below derivations assume only single scattering and only from solute molecules under the approximation that their polarisability far exceeds that of solvent molecules. The Rayleigh approximation ($r_{particle} \ll \lambda_{light}$) is taken as per much of scattering theory to ignore phase changes over the particle size (model validity hence worsens at larger sizes). The formalism begins by considering the in-phase contributions from all solute particles within the illuminated volume to the measured wavefunction (out of phase contributions summing to 0):

$$\Psi(\vec{q}, t) = \int_V d^3r \sum_{j=1}^N \delta(\vec{r} - \vec{r}_j(t)) e^{i\vec{q} \cdot \vec{r}_j} \quad (1)$$

Here the term $\sum_{j=1}^N \delta(\vec{r} - \vec{r}_j(t))$ represents the instantaneous number density at point \vec{r} with \vec{q} as the scattering vector. By considering the volume restriction, this is rewritten as:

$$\Psi(\vec{q}, t) = \sum_{j=1}^N b_j(t) e^{i\vec{q} \cdot \vec{r}_j} \quad (2)$$

$$b_j(t) = \begin{cases} 1, & \text{if } j \in V, \\ 0, & \text{otherwise.} \end{cases} \quad (3)$$

The total number of particles in volume V at time t is given by:

$$N(t) = \sum_{j=1}^N b_j(t) \quad (4)$$

For sufficiently dilute solutions, particle positions can be taken as statistically independent [3] and the autocorrelation can be evaluated:

$$\gamma(\vec{q}, t) = \left\langle \sum_{j=1}^N b_j(0) b_j(t) e^{i\vec{q} \cdot [\vec{r}_j(t) - \vec{r}_j(0)]} \right\rangle \quad (5)$$

The timescale for variation in $b_j(t)$ is simply the timescale for a particle to diffuse with diffusivity D across a length scale L , which goes as $\tau_b \sim \frac{L^2}{D}$. The timescale for variation in the phase goes as [4] $\tau_q \sim (q^2 D)^{-1}$. For visible wavelengths, $q \sim 10^5 \text{ cm}^{-1}$ and $L \sim 0.01 \text{ cm}$ thus $\frac{\tau_b}{\tau_q} \sim (qL)^2$ is of order 10^6 . Having established that variation in $b_j(t)$ is significantly slower than the phase factor, the approximation $b_j(t) \sim b_j(0)$ becomes valid. Applying this to the autocorrelation:

$$\gamma(\vec{q}, t) = \sum_{j=1}^N \langle b_j(0) \rangle \langle e^{i\vec{q} \cdot [\vec{r}_j(t) - \vec{r}_j(0)]} \rangle \quad (6)$$

Noting that the time averaged exponent should be the same for all j (under ergodicity assumptions, time averages represent a full state space exploration [5]) let:

$$F_s(\vec{q}, t) \equiv \langle e^{i\vec{q} \cdot [\vec{r}_j(t) - \vec{r}_j(0)]} \rangle \quad (7)$$

Substituting these newly defined parameters into Eqn. (6):

$$\gamma(\vec{q}, t) = \langle N \rangle F_s(\vec{q}, t) \quad (8)$$

It is often more convenient to work with $F_s(\vec{q}, t)$ given its normalised form, but relation to the canonical autocorrelation is shown for completeness. Using the Fourier transform of property δ functions, $F_s(\vec{q}, t)$ can be related to the probability distribution $G_s(\vec{R}, t)$:

$$F_s(\vec{q}, t) = \int_V d^3 R e^{i\vec{q} \cdot \vec{R}} G_s(\vec{R}, t) \quad (9)$$

$$G_s(\vec{R}, t) = \langle \delta(\vec{R} - [\vec{r}_j(t) - \vec{r}_j(0)]) \rangle \quad (10)$$

$G_s(\vec{R}, t)$ can be considered as the probability density that a particle has been displaced by \vec{R} in time t . Now, information of the stochastic nature of the system can be harnessed through $G_s(\vec{R}, t)$, which is expected to follow a diffusion-like equation [2]. Starting with the simple Brownian motion case:

$$\frac{\partial G_s}{\partial t} = D \nabla^2 G_s \quad (11)$$

Using the Fourier property of derivatives and taking the initial condition $F_s(\vec{q}, 0) = 1$:

$$F_s(\vec{q}, t) = e^{-q^2 D t} \quad (12)$$

1.1 DLS

One way of using the property in Eqn. (12) is to measure the discrete time autocorrelation function at specific scattering angles θ which will have corresponding scattering vectors \vec{q} where $q \equiv |\vec{q}| = \frac{4\pi n}{\lambda} \sin \frac{\theta}{2}$ [6] ($n \approx 1.33$ for water was used in Sec. 2.1). This is precisely what is done in DLS (Dynamic Light Scattering) with the minor caveat that if measurements of the scattering field are made using a camera, they will inherently measure intensity. Following the more thorough discussion in [7] and introducing the free parameter β which encompasses optical effects (primarily coherence), one obtains:

$$f_{DLS}(\vec{q}, t) = 1 + \beta^2 |F_s(\vec{q}, t)|^2 \quad (13)$$

It can be seen then that intensity autocorrelation measurements in DLS will reconstruct $f_{DLS}(\vec{q}, t)$, which decays with characteristic time $\tau_c = \frac{1}{2q^2 D}$. Taking the approximation of spherical particles in a Newtonian Fluid, the Stokes' relation can be employed where $D = \frac{k_B T}{3\pi\eta a}$ for spherical particles of diameter a in a fluid of viscosity η (henceforth particles will assumed to be spherical to make use of the Stokes' relation).

1.2 DDM

DDM (Dynamic Differential Microscopy) [8] makes use of the above stochastic physics in a more subtle way. Instead of measuring scattered light, video footage of the full illuminated sample is collected. A well focused video will show the time evolution of the particle distribution. Although camera frames are quantised by pixels measuring light intensity, it is important to distinguish this intensity from the scattering intensity. Each frame is in fact displaying a “snapshot” of the particle distribution:

$$\rho(\vec{r}, t) = \sum_{j=1}^N \delta(\vec{r} - \vec{r}_j(t)) \quad (14)$$

The DDM algorithm (discussed formally in Sec. 2.2.1) takes the difference between frames, performs a spatial Fourier transform and time averages the absolute value squared (thus constructing the Image Structure Function or ISF):

$$\Delta\rho(\vec{r}, t') = \rho(\vec{r}, t + t') - \rho(\vec{r}, t) \quad (15)$$

$$\text{ISF}(\vec{q}, t') = \langle |\Delta\tilde{\rho}(\vec{q}, t')|^2 \rangle \quad (16)$$

$$\begin{aligned} &= \langle \tilde{\rho}(\vec{q}, t + t')^2 \rangle + \langle \tilde{\rho}(\vec{q}, t)^2 \rangle \\ &\quad - 2 \operatorname{Re} \langle \tilde{\rho}(\vec{q}, t + t') \tilde{\rho}^*(\vec{q}, t) \rangle \end{aligned} \quad (17)$$

Once again making use of the Fourier property of δ functions and noticing that $\langle \rho^2 \rangle$ will evaluate to a constant function of \vec{q} independent of time:

$$\text{ISF}(\vec{q}, t') = 2A'(\vec{q}) - 2 \operatorname{Re} \langle e^{i\vec{q} \cdot [\vec{r}_j(t+t') - \vec{r}_j(t)]} \rangle \quad (18)$$

$$\approx 2A'(\vec{q}) [1 - F_s(\vec{q}, t')] + B(\vec{q}) \quad (19)$$

$$\therefore \text{ISF}(q, t) = A(q) \left[1 - e^{-q^2 Dt} \right] + B(q) \quad (20)$$

DDM has recovered the exponential decay term wrapped in a pre-factor $A(q)$ quantifying the magnitude of the autocorrelation signal, and an additive term $B(q)$ for any background optical effects also scaling with image reciprocal distances. These functions can be reasonably approximated by taking $\text{ISF}(q, 0) = B(q)$ (where $t = 0$ is the first video frame) and

$ISF(q, \infty) = A(q) + B(q)$ (where $t = \infty$ is the final video frame). The structure function can be reduced to a non-vector form through radial averaging which is not expected to reduce information given that particle motion should be isotropic. It is important to note that despite the DDM \vec{q} 's originating from the Fourier transform, they are taken to be equivalent to the more physically meaningful scattering \vec{q} 's interpreted from DLS [8].

1.2.1 Ballistic Motion

The analytical forms for both DLS and DDM measurements have been established in the Brownian domain. The DDM formalism can however be extended to the case of (non-motile) ballistic motion by including a flux term in the diffusion equation for G_s [2]:

$$D\nabla^2 G_s = \frac{\partial G_s}{\partial t} + \vec{v} \cdot \vec{\nabla} G_s \quad (21)$$

$$\Rightarrow F_s(\vec{q}, t) = e^{-q^2 Dt} e^{i\vec{q} \cdot \vec{v}t} \quad (22)$$

$$\Rightarrow ISF(q, t) = A(q) \left[1 - e^{-q^2 Dt} \cos(\vec{q} \cdot \vec{v}t) \right] + B(q) \quad (23)$$

For the case of particles moving under gravity, one expects $v \sim 10^{-2} \mu\text{ms}^{-1}$ with $q \sim 10 \mu\text{m}^{-1}$ thus $\vec{q} \cdot \vec{v} \equiv \omega_{ballistic} \sim 10^{-1} \text{ rads}^{-1}$. Empirically, for micron sized particles, $\tau_c \sim 10 \text{ ms}^{-1}$ which is a significantly faster decay rate than the ballistic oscillatory component. This suggests that graphically recovering $\omega_{ballistic}$ may prove an issue. Drawing again from Berne & Pecora's insights [2], a temporal Fourier transform can be leveraged:

$$1 - \frac{ISF(q, t) - B(q)}{A(q)} \approx e^{-q^2 Dt} \cos(\omega_{ballistic} t) \cos(\omega_{mains} t) \quad (24)$$

$$\begin{aligned} &\equiv F_s^{ballistic}(q, t) \\ &\propto e^{-q^2 Dt} [\cos(\Omega_+ t) + \cos(\Omega_- t)] \end{aligned} \quad (25)$$

The extra $\cos(\omega_{mains} t)$ term has been introduced to account for oscillatory noise from any mains connected devices (camera, ambient lights etc.). Here $\Omega_{\pm} = \omega_{mains} \pm \omega_{ballistic}$ have been defined for convenience.

$$\tilde{F}_s^{ballistic}(q, \omega) \propto \sum_{\sigma=\pm 1} \sum_{\Omega \in \{\Omega_+, \Omega_-\}} \frac{1}{(q^2 D)^2 + (\omega + \sigma \Omega)^2} \quad (26)$$

Temporal Fourier peaks are expected at $\omega = \pm \Omega_{\pm}$. A problem can readily be identified by considering the scales of the frequencies in question: $\omega_{mains} \sim 300 \text{ rads}^{-1} \gg \omega_{ballistic}$ thus $\Omega_{\pm} \approx \pm \omega_{mains}$. Another problem may arise if the oscillatory signals are weak relative to the DC signals, in which case the 0Hz peak dominates the spectrum. These convolution problems will be addressed in Sec. 3.2.2.

1.2.2 Viscoelastic Fluids

It can be shown [9] that for particles suspended in viscoelastic fluids, *sub-diffusive* motion occurs observing the power law:

$$\langle r^2(t) \rangle \sim t^{\beta} \quad (27)$$

$$\Rightarrow F_s(q, t) \sim e^{-X q^{\alpha} t^{\beta}} \text{ for } 0 < \beta < 1 \quad (28)$$

In the Newtonian fluid case: $X \equiv D$, $\alpha = 2$ & $\beta = 1$. It is also theoretically possible to recover the Viscoelastic Modulus $G^*(\omega)$ [10], but this proves difficult empirically. Probing the viscoelasticity is nonetheless possible by observing the sub-exponential time evolution of $F_s(q, t)$.

1.2.3 Particle Mixtures

It is shown in [11] that for a multi-modal particle suspension of M different non-interacting species, the structure function components can be re-written as:

$$A(q) = \sum_{i=1}^M A_i(q) \quad (29)$$

$$F_s(q, t) = \sum_{i=1}^M \frac{A_i(q)}{A(q)} e^{-q^2 D_i t} \quad (30)$$

$$\Rightarrow ISF_{multi} = A(q) [1 - F_s(q, t)] + B(q) \quad (31)$$

It is expected that the ratios of $A_i(q)$ will reflect the relative particle concentrations. If the particle sizes are sufficiently different such that the $\tau_c^{(i)}$ are on different timescales, the ISF can be approximated by the according particle's contribution *only*, in the according time regime.

2 Experimental

2.1 DLS

The optical rig was setup as in Fig. 1 and the laser beam aligned. Laboratory lights were turned off and a black cloth was used to shield the optical rig from other ambient light sources. Colloid solutions were prepared using Polystyrene Microspheres (sourced from *Polysciences, Inc.*) in Milli-Q water. Successful DLS runs were achieved with particles of diameter 0.51 μm (1000x dilution), 0.746 μm (100x dilution) and 1.06 μm (1000x dilution). The glass sample slide was rinsed in ethanol before each run and then screwed into the sample holder. The following scattering angles were selected for measurement:

$\theta(\circ)$	$\delta\theta/\theta(\%)$	$q(\mu\text{m}^{-1})$	$\delta q/q(\%)$
26.6	0.102	6.1	5.7
30.0	0.087	6.8	5.0
35.0	0.069	7.9	3.7
40.0	0.055	9.0	2.9
45.0	0.044	10.1	2.4
48.0	0.038	10.7	2.0
50.0	0.034	11.1	1.9

Table 1: Scattering Angles and Wavevectors with uncertainties

The above errors were propagated from the measurement uncertainties (see Fig. 2 and Fig. 3) as follows:

$$\theta = \arctan \frac{a}{b}$$

$$\delta\theta = \frac{\sqrt{\left(\frac{\partial\theta}{\partial a}\delta a\right)^2 + \left(\frac{\partial\theta}{\partial b}\delta b\right)^2}}{a^2 + b^2} \quad (32)$$

$$\delta\left(\sin\frac{\theta}{2}\right) = \frac{1}{2} \cos\frac{\theta}{2} \delta\theta$$

$$\frac{\delta q}{q} = \frac{\delta\left(\sin\frac{\theta}{2}\right)}{\sin\frac{\theta}{2}} \quad (33)$$

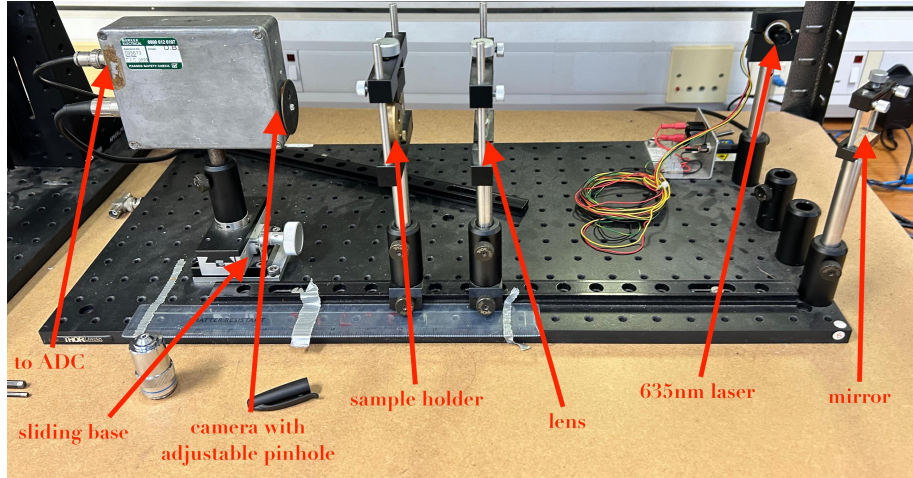


Figure 1: DLS set-up side view

Scattered intensity was recorded using a USB camera through an ADC (Analogue-Digital-Converter) and processed using a *PicoTech* data acquisition package. Data was recorded for 10 s at 1 ms intervals. The raw voltage data was pre-processed using the `signal.butter` and `signal.filtfilt` methods from the python `scipy` library [12] to remove noise in the ~ 50 Hz range (mains sources). The data was assumed to behave like Eqn. (13), but with no knowledge of β , was fit logarithmically to a more naive form: $f_{DLS}(q, t) \sim e^{-\frac{t}{\tau_c}}$ with $\tau_c = \frac{1}{2q^2D}$. The characteristic time was extracted from the linear fit gradient using the first 30 data points (noise effects were found to grow over time) using the `scipy.stats.linregress` module, which also returned the standard error in the fitted gradient (from which σ_{τ_c} is recovered). The particle diameter was thus recovered with according error:

$$a = \frac{2q^2\tau_c k_B T}{3\pi\eta} \quad (34)$$

$$\frac{\delta a}{a} = \sqrt{\left(\frac{\sigma_{\tau_c}}{\tau_c}\right)^2 + \left(2\frac{\delta q}{q}\right)^2} \quad (35)$$

The nominal values of laser wavelength, water viscosity, and room temperature (measured with a laser thermometer) were taken to have negligible error and were used for all data analyses including DDM ($\lambda = 635$ nm, $\eta = 8.9 \times 10^{-4}$ Pa s, $T = 296$ K).

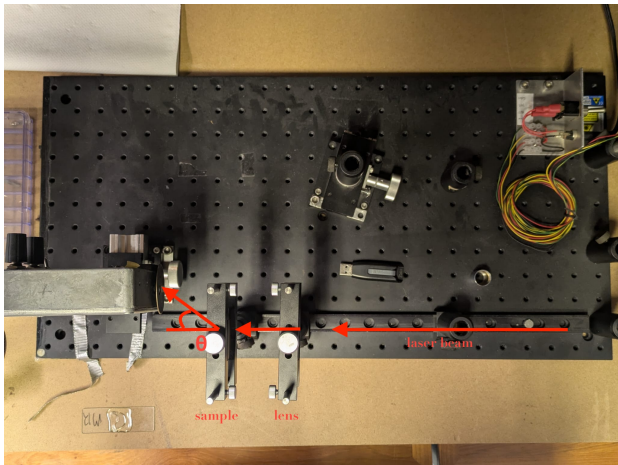


Figure 2: DLS set-up top view

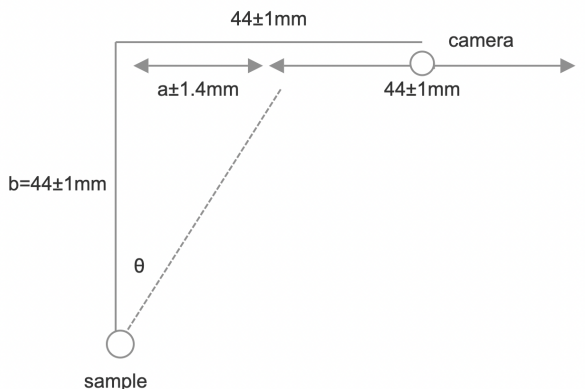


Figure 3: DLS top view schematic

2.2 DDM

The optical rig was setup as in Fig. 4. Unlike DLS, laboratory lights were left on and no light shielding was used. Three lenses were used: x10, x20 & x40 magnification. For each, a calibration ruler was used to obtain a pixel to real space resolution. The calibration was repeated after apparatus changes (rotating to Fig. 7 setup). The values were in the range:

Lens	$\times 10$	$\times 20$	$\times 40$
$\mu\text{m}/\text{px}$	0.45	0.23	0.13

Table 2: Lens Calibration

Colloid solutions were prepared as in DLS now with diameters: 0.51 μm , 0.746 μm , 1.06 μm , 2.07 μm and 3.1 μm . It was found that for larger particles, a higher dilution ($>1000x$) helped to prevent particles from clustering together, thus behaving as effectively larger particles (creating an effective polydispersity) and skewing data - Fig. 6. Particle solutions were pipetted under thin glass slides as in Fig. 5 (reducing the orthogonal length scale is assumed to reduce multiple scattering effects by restricting particles to a plane).

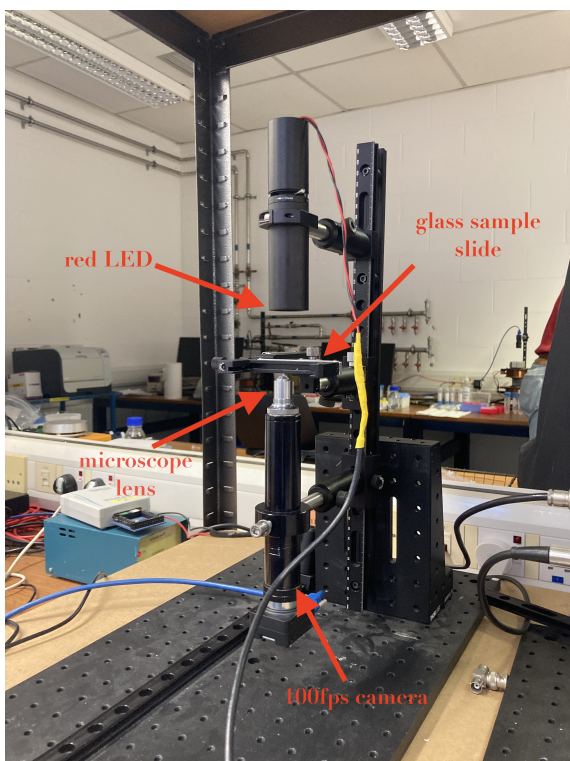


Figure 4: DDM vertical setup



Figure 5: DDM glass sample slide

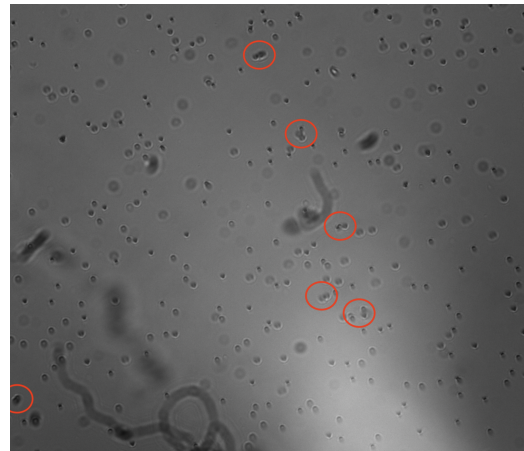


Figure 6: 2.07 μm (1000x dilution) clustering

Looking at Fig. 5, air bubbles can be seen beneath the glass slide. Despite sealing the slides with UV curing glue, it was found that over time, the seal would allow air bubbles (either in the solution from pipetting or from outside) to move under the slide. Such samples were disposed of as the air bubble motion caused drift currents in the fluid.

With slides loaded onto the microscopy stage, the LED was aligned to achieve Kohler (flat intensity) illumination [13]. Specks of dirt and other immobile optical artefacts as seen in Fig. 6 were not of any concern given the differential nature of DDM. Videos were recorded at

the camera's native framerate of 100 FPS, the maximum rate at which the computer could write data without buffer errors, for durations between 3 s to 6 s. The camera was operated using a *PointGrey FlyCap* video acquisition package.

2.2.1 DDM Algorithm

From the theoretical discussions in Sec. 1.2, each frame can be considered to be a 2D particle distribution density. The DDM algorithm is outlined below in pseudo-code:

1. Load video data into array of NxN matrices (N=1024 pixels)
2. Preprocess each frame (to sharpen the particle distribution function):
 - take `background` as average over all frames
 - apply gaussian filter to `background`
 - subtract `background` from all frames
3. Generate log-spaced array of lag times with `pointsPerDecade` τ_s per power of 10 (want more frames close together near $t = 0$)
4. Parallelised over all τ compute:
 - create `initialTimes` array spaced in steps of $\max((\text{len(frames)} - \tau) / \text{maxNCouples}, 1)$ where `maxNCouples` refers to max no. pairs of frames for which `FFTDiff` is evaluated
 - for each t in `initialTimes` perform $\text{FFTDiff} = |\text{FFT}[\rho(\vec{r}, t) - \rho(\vec{r}, t + \tau)]|^2$
 - compute `FFTDiff` averaged over all t in `initialTimes`
 - obtain $ISF(\vec{q}, \tau)$
5. Parallelised over all τ compute:
 - radially average $ISF(\vec{q}, \tau)$ in \vec{q} space
 - obtain $ISF(q, \tau)$

The syntactical intricacies of the algorithm will not be discussed here but it was found that with Parallelisation, algorithm runtimes were reduced approximately fourfold per video. All analyses were run with `maxNCouples`=50 and `pointsPerDecade`=60.

The following sections detail primarily how data was processed differently under different schemes, but the above algorithm was always used.

2.2.2 Brownian

For each Brownian motion video the following was done. The logarithm of the ISF data was fitted to the logarithm of the analytical form of Eqn. (20) using the `curve_fit` method from `scipy.optimize` with free fit parameters $A(q), B(q)$ & $\tau_c(q)$. Fitting was done in log-space to yield a closer to linear form. A plot of $\tau_c(q)$ against q (on log axes) was produced to seek a linear region following $\log \tau_c(q) = -\log D - \alpha \log(q)$ (with $\alpha_{theory} = 2$). The optimal range of $[q_{min}, q_{max}]$ was identified heuristically by minimising $|2 - \alpha|$ while still covering a large data range. Within this reduced range, the parameters $A(q), B(q)$ & $\tau_c(q)$ were fit again and a final plot of $\tau_c(q)$ against q was produced with standard fit errors in σ_{τ_c} as error bars.

From this plot, the diffusivity D was fit (with α set to 2) by minimising $-\log D_{fit} - 2 \log q - \log \tau_c^{(data)}$. The σ_{τ_c} were used to weight the fitting of D ($\chi^2 = \sum_i (\frac{y_i - f(x_i)}{\sigma_i})^2$). The standard fit error in D was propagated into the error for diameter:

$$\sigma_a = \frac{a}{D} \sigma_D \quad (36)$$

DDM was run on samples of diameter and dilution: 0.51 μm (1000x), 0.746 μm (5000x), 1.06 μm (5000x), 2.07 μm (5000x) and 3.1 μm (5000x).

2.2.3 Ballistic

The apparatus was rotated onto its side (Fig. 7) such that gravity would exert a uni-directional flux on the particle suspension. The $A(q)$ and $B(q)$ functions were approximated using the first frame & last frame “trick” detailed in Sec. 1.2 and following Eqn. (24), $F_s^{\text{ballistic}}(q, t)$ was recovered and Fourier transformed in t . The `scipy signal.butter` and `signal.filtfilt` methods were used first to bandfilter in the 48-50Hz range (to filter mains noise) and then to high-pass with threshold $f_{\text{thresh}} = 0.001\text{Hz}$ (to filter DC signals but keep the $\pm\omega_{\text{ballistic}}$ peaks near 0Hz).

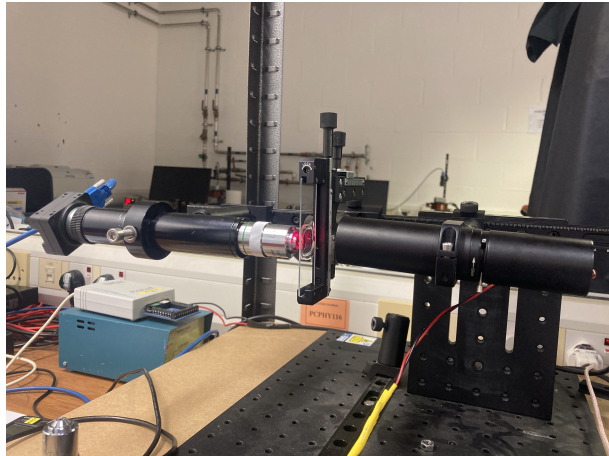


Figure 7: Ballistic DDM setup

DDM was run on the same samples as for Brownian motion (Sec. 2.2.2). The temporal Fourier spectra were plotted for select q values within the previously obtained q-range.

2.2.4 Viscoelastic

Samples were prepared using Pluronic F127 polymer dissolved in Milli-Q water. Solutions of 5%, 10% and 20% polymer (by weight) were made and only 2.07 μm beads were used in 1000x dilution. The vials were then left on a shaker overnight to allow the solutions to homogenise (following a similar procedure to [14]). After pipetting the fluid under the glass slide, the sample was left for ~ 1 hour to allow stresses to relax. The slides were then mounted onto the stage in the vertical setup (Fig. 4). With video data collected, $F_s(q, t)$ was recovered using the first frame & last frame method. For select q values, $F_s(q, t)$ was plotted against time on a semi-log scale (y-axis logarithmic only) to display the non-linearity arising from Eqn. (28).

2.2.5 Particle Mixtures

Samples were prepared with mixtures of 0.51 μm & 1.06 μm , 0.746 μm & 2.07 μm , 1.06 μm & 2.07 μm and 2.07 μm & 3.1 μm (with the smaller particle in each binary mixture at 2000x dilution and the larger at 4000x). The concentrations were chosen to test the hypothesis that the ratio of $A_i(q)$ would be equal to the concentration ratio. The Fig. 4 vertical setup was used for DDM runs. The video data was processed similar to Sec. 2.2.2 but now fitting to the theoretical bi-modal ISF as in Eqn. (31). The method of first identifying the optimal $[q_{min}, q_{max}]$ range was again employed and refitting was done in the reduced range. Extraction of diffusivities and particle sizes followed just as in Sec. 2.2.2.

3 Results and Discussion

3.1 DLS

The DLS data exhibited a lot of variability and de-noising proved difficult given the variety of oscillatory artefacts in the data (beyond the targeted $\sim 50\text{Hz}$ band) as seen in Fig. 8 and Fig. 9.

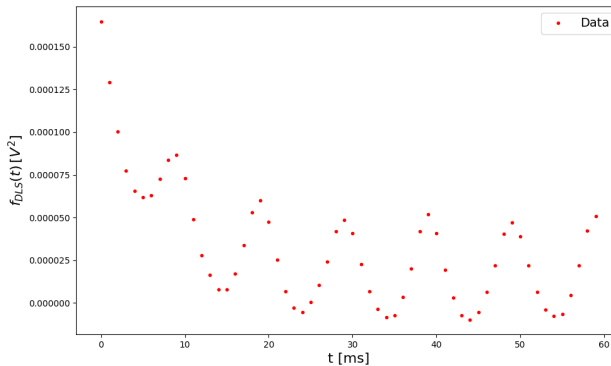


Figure 8: $\sim 100\text{Hz}$ noise at 50° scattering for 0.51 μm colloids

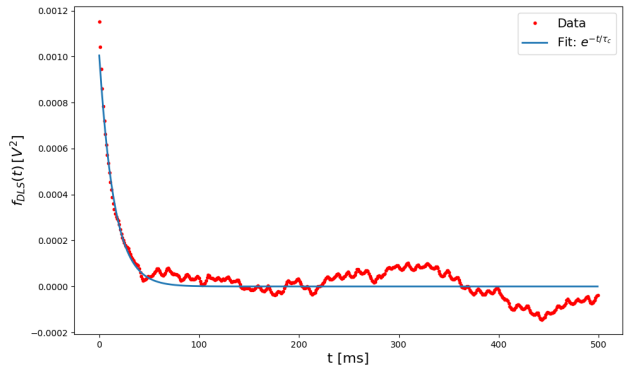


Figure 9: Higher order oscillatory noise at 45° scattering for 0.51 μm colloids

Nonetheless, relaxation time and diameter estimates were extracted for the more successfully de-noised data. The linear fits are shown in Fig. 10, 11 & 12 for select scattering angles (scattering at angles wider than 45° proved problematic due to poor signal to noise ratio).

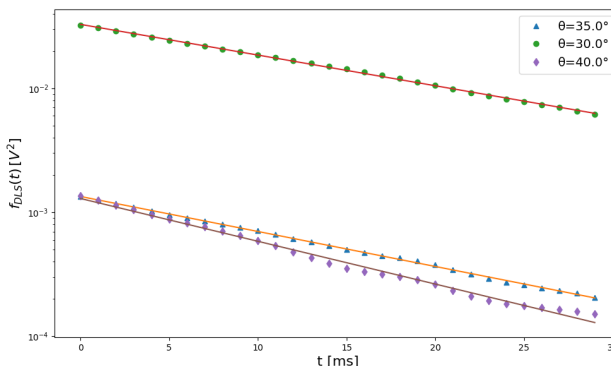


Figure 10: 0.51 μm colloids intensity autocorrelation

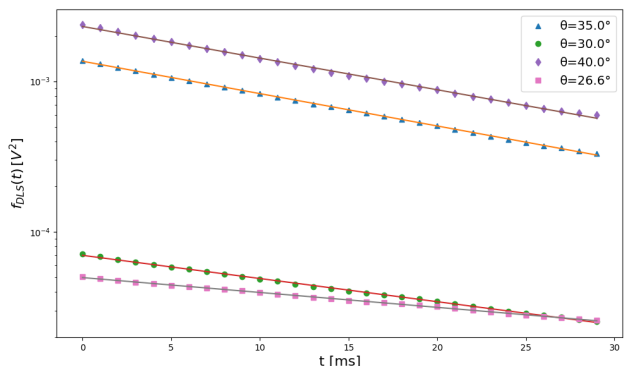


Figure 11: 0.746 μm colloids intensity autocorrelation

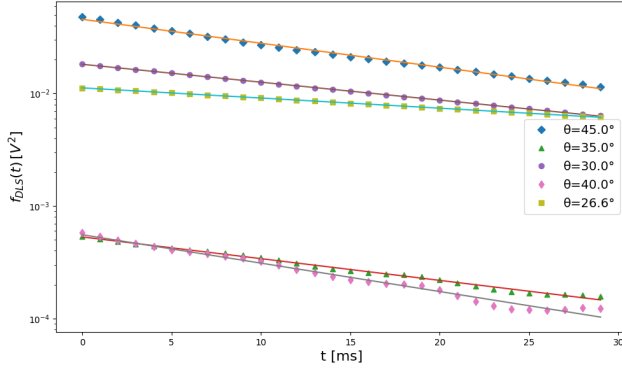


Figure 12: $1.06\text{ }\mu\text{m}$ colloids intensity autocorrelation

To yield final estimates of diameter, the standard errors in τ_c were propagated as in Eqn. (35) and then the standard deviation in the list of a values (σ_a) was summed in quadrature with the individual diameter uncertainties (δa_i):

$$\delta a_{total} = \sqrt{\frac{\sigma_a^2}{N} + \sum_{i=1}^N (\delta a_i)^2} \quad (37)$$

(Only the scatter angles displayed in Fig. 10, 11 & 12 were used for this calculation)

a_{true} (μm)	a_{data} (μm)	δa_{data} (μm)
0.51	0.45	0.07
0.746	0.71	0.14
1.06	0.77	0.16

Table 3: Comparison of true and estimated diameters with uncertainties.

The data shows good agreement for the smaller sizes yet underestimates quite substantially for the $1.06\text{ }\mu\text{m}$ beads. This was attributed to larger beads exhibiting slower brownian motion resulting in worse signal to noise ratios. These initial cruder DLS estimates provided intuition for the length scales expected when conducting DDM.

3.2 DDM

3.2.1 Brownian

The Brownian motion data for DDM was of varying success. The ISF was constructed using the algorithm in Sec. 2.2.1 and one such ISF heat-map is shown in Fig. 13.

Diameter calculations were found to often overshoot which was attributed to clustering and other retarding interactions which would increase the effective particle size. The dynamic q-range selection proved efficient and for all particle sizes, a substantial range was recovered with $\alpha_{data} = 2.00 \pm 0.01$ as in Fig. 14.

Once the ISF parameters were refit in the optimised q-range, the logarithmic $\tau_c(q)$ plots (2 such examples displayed in Fig. 17) were produced.

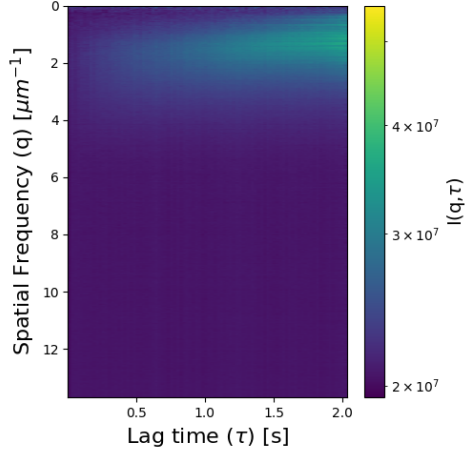


Figure 13: $0.51\text{ }\mu\text{m}$ Image Structure Function

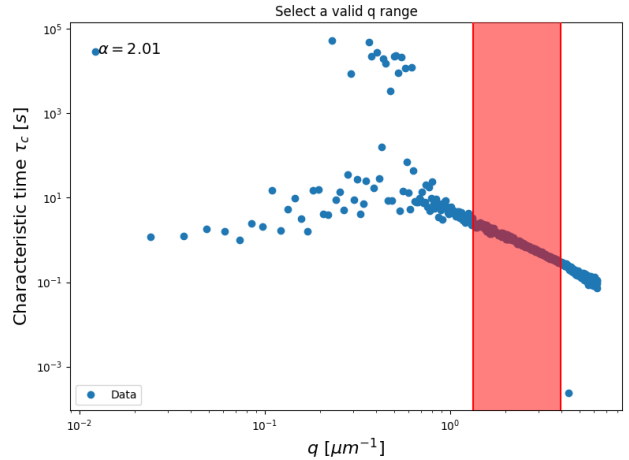


Figure 14: q -range for $2.07\text{ }\mu\text{m}$ colloids

(The 0.51 , 1.06 & $3.1\text{ }\mu\text{m}$ plots - not shown below - yielded estimates of $a = 0.50 \pm 0.02\text{ }\mu\text{m}$, $a = 1.16 \pm 0.04\text{ }\mu\text{m}$ & $a = 4.63 \pm 0.07\text{ }\mu\text{m}$ respectively)

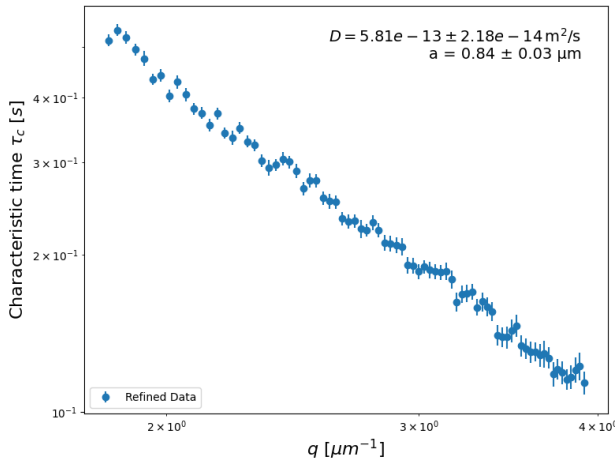


Figure 15: $\tau_c(q)$ vs. q for $0.746\text{ }\mu\text{m}$ colloids with $0.234\text{ }\mu\text{m}/\text{px}$ ($\times 20$ lens).

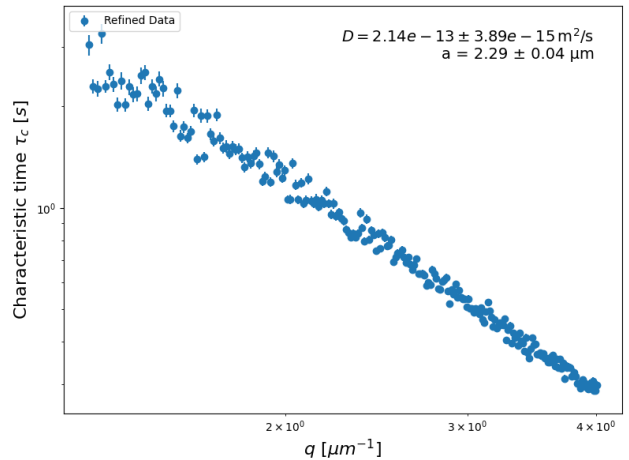


Figure 16: $\tau_c(q)$ vs. q for $2.07\text{ }\mu\text{m}$ colloids with $0.504\text{ }\mu\text{m}/\text{px}$ ($\times 10$ lens).

Figure 17: Characteristic times $\tau_c(q)$ for micron-sized colloids using DDM.

The expected linearity is displayed with tight error bars. However, the nominal diameters are not included in the estimated error bounds. Error propagations through least squares heavily reduce the estimated errors (due to central value averaging) thus explaining the small error bars. Gradient (and thus Diffusivity) errors could alternatively be estimated through a max/min gradient calculation, but given the tightness of the error bars, this would unlikely yield a wider error bound. There are also various *hyperparameters* in the DDM algorithm (namely: `maxNCouples`, and `pointsPerDecade`) which can be varied to examine the stability of the estimated variables. Another area for further experimentation is the filtering method used - this procedure used a gaussian filtering technique detailed in Sec. 2.2.1. The gaussian filter noticeably reduced noise as shown in Fig. 18 & 19.

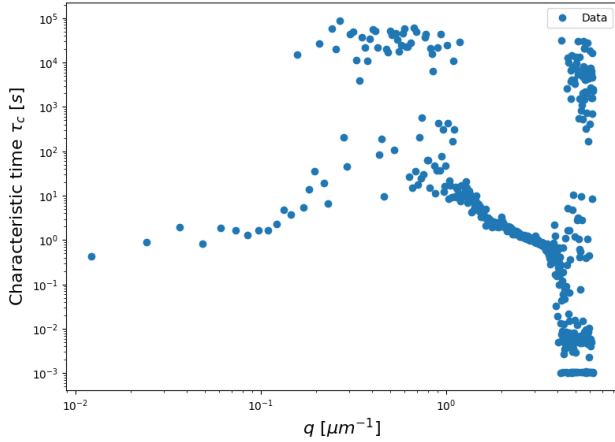


Figure 18: $3.1\text{ }\mu\text{m}$ $\tau_c(q)$ fitting *before* gaussian filter

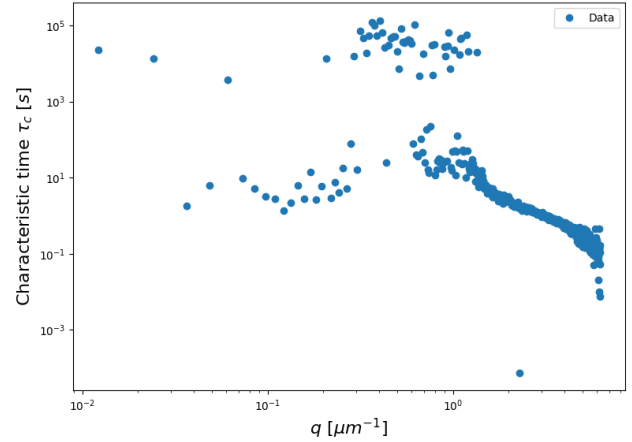


Figure 19: $3.1\text{ }\mu\text{m}$ $\tau_c(q)$ fitting *after* gaussian filter

3.2.2 Ballistic

The *renormalised* autocorrelation functions $F_s(q, t)$ were successfully recovered and are shown in Fig. 22 for two particle sizes *before* band-filtering at $\sim 50\text{Hz}$.

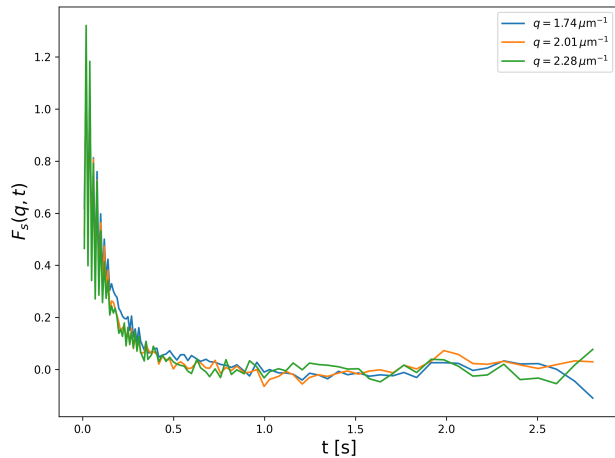


Figure 20: $0.51\text{ }\mu\text{m}$ colloids renormalised $F_s(q, t)$

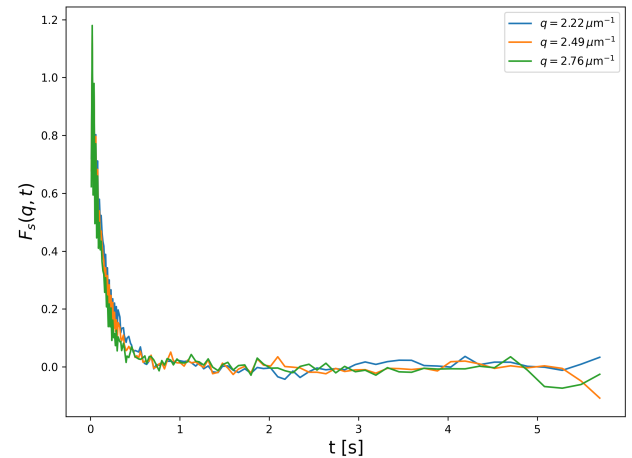


Figure 21: $1.07\text{ }\mu\text{m}$ colloids renormalised $F_s(q, t)$

Figure 22: $F_s^{ballistic}(q, t)$ *before* band-filtering at $\sim 50\text{Hz}$

The figures display characteristic decay of the correct order (given previous estimates) and clearly display a high frequency noise component presumably from mains.

The temporal spectra of these functions yielded promising shapes. Before high-passing, the spectra were all dominated by the DC peak at 0Hz but high-passing revealed the expected doublets. The according spectra for Fig. 22 are shown in Fig. 25.

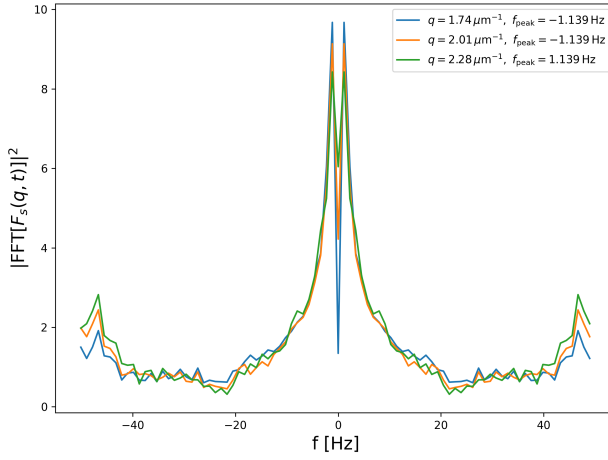


Figure 23: $0.51\text{ }\mu\text{m}$ colloids temporal spectrum

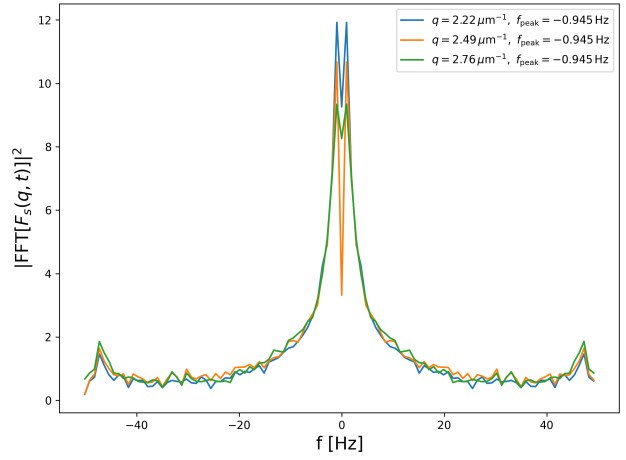


Figure 24: $1.07\text{ }\mu\text{m}$ colloids temporal spectrum

Figure 25: Temporal Fourier spectra for micron-sized colloids in ballistic motion

A crude estimate of the terminal velocities is given by $v_t \approx \frac{2\pi|f_{peak}|}{q} \sim 1\text{ }\mu\text{m s}^{-1}$ which is significantly faster than estimates from the Stoke's law $v_t = \frac{2r^2(\rho - \rho_{fluid})g}{9\eta}$ which give $v_t \sim 10^{-2}\text{ }\mu\text{m s}^{-1}$ (taking $\rho_{colloid} \equiv \rho \approx 1.05\text{ g cm}^{-3}$ as quoted by [15]). If the spectra reconstructions are faithful to the expected behaviour, these heightened speeds are very likely the effect of air bubbles in the medium. Nonetheless, an interesting extension of DDM was tested.

3.2.3 Viscoelastic

The semi-logged plots of $F_s(q, t)$ are shown in Fig. 28 & 30.

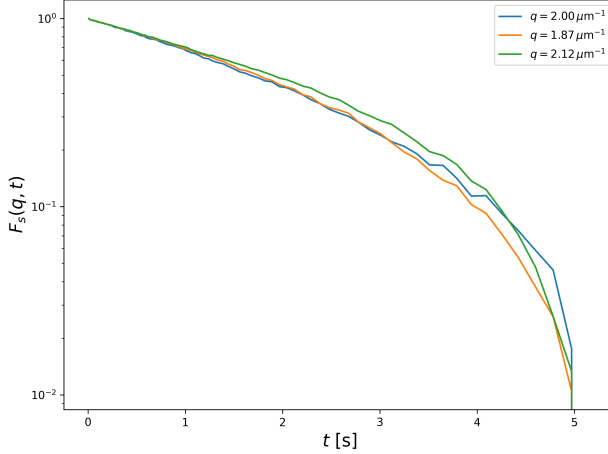


Figure 26: 5% Pluronic F127 solution

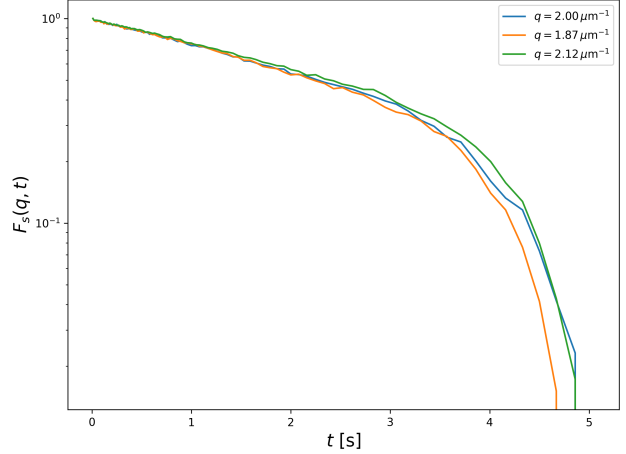


Figure 27: 10% Pluronic F127 solution

Figure 28: Sub-diffusive behavior for $2.07\text{ }\mu\text{m}$ colloids (part 1).

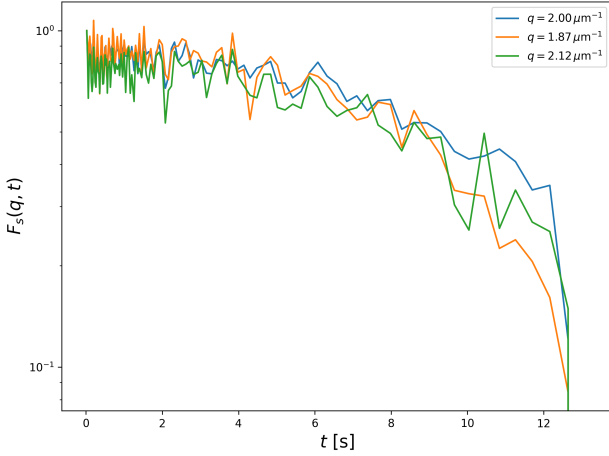


Figure 29: 20% Pluronic F127 solution

Figure 30: Sub-diffusive behavior for 2.07 μm colloids (part 2).

All three plots display the expected *sub-exponential* decay in time. Fig. 29 is noticeably noisier than the rest which is attributed to the higher concentration polymer solution taking longer to relax from stresses (thus particle motion was still being driven by motion of the medium).

3.2.4 Particle Mixtures

Fitting to the bi-modal ISF - Eqn. (31) - proved difficult on most samples yet two distinct populations were consistently seen in the fitting process. The main difficulty arose in focusing the lens onto a focal plane containing both populations well resolved. Of the four samples run, the best results came from the 0.746 μm & 2.07 μm mixture shown in Fig. 33.

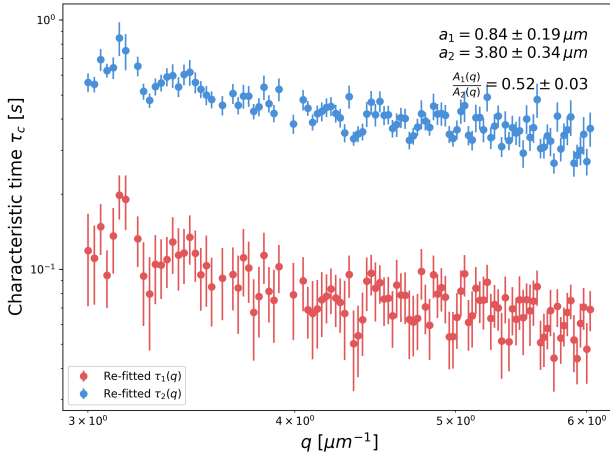


Figure 31: Bi-modal population of characteristic times

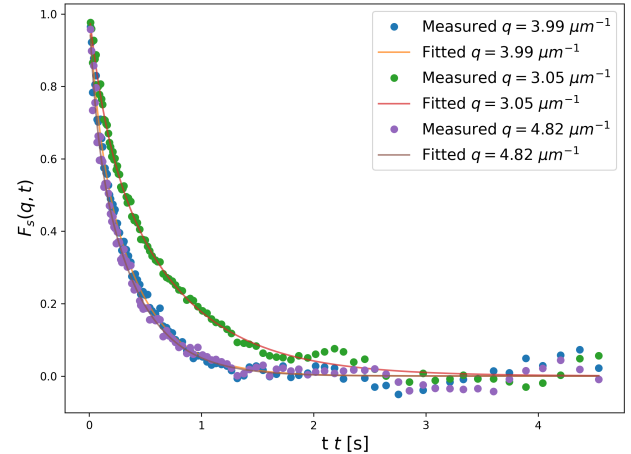


Figure 32: Fitted vs Empirical $F_s(q,t)$ using bi-modal model

Figure 33: 0.746 μm & 2.07 μm colloid bi-modal mixture

Not only did this sample recover a correct estimate for the smaller of the particle diameters, DDM also recovered the expected $A_i(q)$ ratio of 1:2 given the relative particle concentrations. The fits for $F_s(q,t)$ shown in Fig. 32 give further validity to the theoretical form of the bimodal ISF. A future area of experimentation could be the use of EDF (Extended Depth of Field [16]) to stack images from different focal planes to help circumvent focusing issues.

4 Conclusions

The efficacy of both DLS (Dynamic Light Scattering) and DDM (Differential Dynamic Microscopy) was tested through the extraction of diffusivity and diameter measures for colloids undergoing Brownian motion in a viscous fluid. For colloids of size $0.51\text{ }\mu\text{m}$, $0.746\text{ }\mu\text{m}$, $1.06\text{ }\mu\text{m}$, DLS yielded estimates of $0.45 \pm 0.07\text{ }\mu\text{m}$, $0.71 \pm 0.14\text{ }\mu\text{m}$, $0.77 \pm 0.16\text{ }\mu\text{m}$ respectively. For the same three sizes, DDM yielded estimates of $0.50 \pm 0.02\text{ }\mu\text{m}$, $0.84 \pm 0.03\text{ }\mu\text{m}$, $1.16 \pm 0.04\text{ }\mu\text{m}$. DDM was additionally run on $2.07\text{ }\mu\text{m}$ and $3.1\text{ }\mu\text{m}$ colloids, which yielded diameter estimates of $2.29 \pm 0.04\text{ }\mu\text{m}$ and $4.63 \pm 0.07\text{ }\mu\text{m}$. Both methods struggled with larger colloids due to model limitations, including ignoring multiple scattering and polydispersity, and the Rayleigh approximation (all of which are model assumptions whose validity worsens with larger particles). More exotic behaviours were studied using the DDM formalism including ballistic motion, Brownian motion in a viscoelastic fluid and finally bi-modal particle solutions under Brownian motion. The vast capabilities for data retrieval from the DDM method were demonstrated under these scenarios. Significant improvements were also made to the DDM Algorithm itself yielding \sim fourfold runtime improvements.

References

- [1] P. N. Pusey. ‘Dynamic light scattering by non-equilibrium colloidal suspensions’. In: *Journal of Physics: Condensed Matter* 6.23A (1994), A29–A37. DOI: 10.1088/0953-8984/6/23A/004.
- [2] John Berne and Robert Pecora. *Dynamic Light Scattering: With Applications to Chemistry, Biology, and Physics*. Dover Publications, 2000. ISBN: 9780486431595.
- [3] P. A. Fleury, W. B. Daniels and J. M. Worlock. ‘Density and Temperature Dependence of Intermolecular Light Scattering in Simple Fluids’. In: *Phys. Rev. Lett.* 27 (22 Nov. 1971), pp. 1493–1496. DOI: 10.1103/PhysRevLett.27.1493. URL: <https://link.aps.org/doi/10.1103/PhysRevLett.27.1493>.
- [4] J. Böheim, W. Hess and R. Klein. ‘Depolarized light scattering from interacting brownian spheres’. In: *Zeitschrift für Physik B Condensed Matter* 32.2 (1979), pp. 237–243. DOI: 10.1007/BF01320119. URL: <https://doi.org/10.1007/BF01320119>.
- [5] Mark Tuckerman. *Statistical Mechanics: Algorithms and Computations*. Oxford, UK: Oxford University Press, 2002. ISBN: 978-0198508363.
- [6] Miroslaw Jonasz and Georges R. Fournier. ‘Chapter 4 - Measurements of light scattering by particles in water’. In: *Light Scattering by Particles in Water*. Ed. by Miroslaw Jonasz and Georges R. Fournier. Amsterdam: Academic Press, 2007, pp. 145–265. ISBN: 978-0-12-388751-1. DOI: <https://doi.org/10.1016/B978-012388751-1/50004-1>. URL: <https://www.sciencedirect.com/science/article/pii/B9780123887511500041>.
- [7] Peter N. Pusey and W. van Megen. ‘Two-colour Dynamic Light Scattering’. In: *Physica A: Statistical Mechanics and its Applications* 82.2 (1976), pp. 321–346. DOI: 10.1016/0378-4371(76)90064-5. URL: https://www.researchgate.net/profile/Peter-Pusey/publication/241403501_Two-colour_Dynamic_Light_Scattering/links/5703a35808aebac127083bf/Two-colour-Dynamic-Light-Scattering.pdf.
- [8] Roberto Cerbino and Veronique Trappe. ‘Differential Dynamic Microscopy: Probing Wave Vector Dependent Dynamics with a Microscope’. In: *Phys. Rev. Lett.* 100 (18 May 2008), p. 188102. DOI: 10.1103/PhysRevLett.100.188102. URL: <https://link.aps.org/doi/10.1103/PhysRevLett.100.188102>.

- [9] Kheder Suleiman et al. ‘Confinement effect on diffusion dynamics in active viscoelastic environments’. In: *The European Physical Journal B* 97.49 (2024), pp. 1–12. DOI: 10.1140/epjb/s10051-024-00685-5. URL: <https://link.springer.com/article/10.1140/epjb/s10051-024-00685-5>.
- [10] W. W. Eaton et al. ‘Viscoelasticity of Complex Fluids: Techniques and Applications’. In: *PubMed* 198 (94975 2009). URL: <https://pubmed.ncbi.nlm.nih.gov/19894975/>.
- [11] Joe J. Bradley et al. ‘Correction: Sizing multimodal suspensions with differential dynamic microscopy’. In: *Soft Matter* 20.15 (2024), p. 3376. DOI: 10.1039/d4sm90050b. URL: <https://pmc.ncbi.nlm.nih.gov/articles/PMC11022541/>.
- [12] Pauli Virtanen et al. ‘SciPy 1.0: Fundamental Algorithms for Scientific Computing in Python’. In: *Nature Methods* 17.3 (2020), pp. 261–272. DOI: 10.1038/s41592-019-0686-2. URL: <https://www.nature.com/articles/s41592-019-0686-2>.
- [13] Manish Saxena, Gangadhar Eluru and Sai Siva Gorthi. ‘Structured illumination microscopy’. In: *Adv. Opt. Photon.* 7.2 (June 2015), pp. 241–275. DOI: 10.1364/AOP.7.000241. URL: <https://opg.optica.org/aop/abstract.cfm?URI=aop-7-2-241>.
- [14] Filipe E. Antunes et al. ‘Gels of Pluronic F127 and nonionic surfactants from rheological characterization to controlled drug permeation’. In: *Colloids and Surfaces B: Biointerfaces* 87.1 (2011), pp. 42–48. ISSN: 0927-7765. DOI: <https://doi.org/10.1016/j.colsurfb.2011.04.033>. URL: <https://www.sciencedirect.com/science/article/pii/S0927776511002402>.
- [15] Thermo Fisher Scientific. *Useful Latex Bead Formulae*. Accessed: 2025-03-14. URL: <https://www.thermofisher.com/us/en/home/life-science/cell-analysis/qdots-microspheres-nanospheres/idc-surfactant-free-latex-beads/latex-bead-technical-overview/useful-latex-bead-formulae.html>.
- [16] ‘E2E-BPF Microscope: Extended Depth-of-Field Microscopy Using Band-Pass Filtering’. In: *Nature Communications* 14.1 (2023), p. 3492. DOI: 10.1038/s41377-023-01300-5. URL: https://www.nature.com/articles/s41377-023-01300-5?utm_source=chatgpt.com.